The local hole: a galaxy underdensity covering 90 per cent of sky to ≈200 Mpc

Jonathan H. W. Wong,[1,2]⋆ T. Shanks [ID],[1] N. Metcalfe[1] and J. R. Whitbourn[1]

[1]*Centre for Extragalactic Astronomy, Department of Physics, Durham University, South Road, Durham DH1 3LE, UK*
[2]*Jodrell Bank Centre for Astrophysics, Department of Physics and Astronomy, University of Manchester, Oxford Road, Manchester M13 9PL, UK*

ABSTRACT

We investigate the 'Local Hole', an anomalous underdensity in the local galaxy environment, by extending our previous galaxy K-band number-redshift and number-magnitude counts to ≈90 per cent of the sky. Our redshift samples are taken from the 2MASS Redshift Survey (2MRS) and the 2M++ catalogues, limited to $K < 11.5$. We find that both surveys are in good agreement, showing an $\approx 21 - 22$ per cent underdensity at $z < 0.075$ when compared to our homogeneous counts model that assumes the same luminosity function (LF) and other parameters as in our earlier papers. Using the Two Micron All Sky Survey (2MASS) for $n(K)$ galaxy counts, we measure an underdensity relative to this model of 20 ± 2 per cent at $K < 11.5$, which is consistent in both form and scale with the observed $n(z)$ underdensity. To examine further the accuracy of the counts model, we compare its prediction for the fainter $n(K)$ counts of the Galaxy and Mass Assembly (GAMA) survey. We further compare these data with a model assuming the parameters of a previous study where little evidence for the Local Hole was found. At $13 < K < 16$, we find a significantly better fit for our galaxy counts model, arguing for our higher LF normalization. Although our implied underdensity of ≈ 20 per cent means local measurements of the Hubble Constant have been overestimated by ≈ 3 per cent, such a scale of underdensity is in tension with a global ΛCDM cosmology at an $\approx 3\sigma$ level.

Key words: cosmological parameters – distance scale.

1 INTRODUCTION

Distance scale measurements of the expansion rate of the Universe or Hubble's Constant, H_0, have improved significantly over recent years. For example, estimates of H_0 calculated by Riess et al. (2016) find the best-fitting value of $H_0 = 73.24 \pm 1.74 \, \mathrm{km \, s^{-1} \, Mpc^{-1}}$, a quoted accuracy of 2.4 per cent. However, this result is in serious tension with H_0 predictions made through ΛCDM model fits to the Planck CMB Power Spectrum. This 'early Universe' measurement yields a value of $H_0 = 67.4 \pm 0.5 \, \mathrm{km \, s^{-1} \, Mpc^{-1}}$ (Planck Collaboration VI 2018), which presents a tension at the $3 - 4\sigma$ level with measurements made using the local distance scale (see also Riess et al. 2018b).

These authors recognize the possibility that a source of the $\sim$ 9 per cent discrepancy between the H_0 measurements is unaccounted systematic uncertainties in one of, or both of the distance scale and early Universe approaches. However, an alternative proposal lies in studies of the galaxy distribution in the local Universe by Shanks (1990), Metcalfe et al. (1991, 2001), Frith et al. (2003), and Busswell et al. (2004), who find evidence for an underdensity or 'Local Hole' stretching to $150 - 200 \, h^{-1}$ Mpc in the local galaxy environment.

Notably, Whitbourn & Shanks (2014; hereafter WS14) suggest that the tension in H_0 measurements may arise from the outflow effects of the Local Hole. They find a detected underdensity of $\approx 15 \pm 3$ per cent in number-magnitude counts $n(m)$ and redshift

distributions $n(z)$, measured relative to a homogeneous model over a $\sim 9000 \, \mathrm{deg^2}$ area covering the NGC and SGC. This underdensity is most prominent at $K < 12.5$ and leads to an $\sim 2 - 3$ per cent increase in H_0 which alleviates the tension to a 5 per cent level. Further, Shanks, Hogarth & Metcalfe (2019a) suggested that Gaia DR2 parallaxes might not have finally confirmed the Galactic Cepheid distance scale as claimed by Riess et al. (2018b) and could at least superficially, help reduce the overall tension to $<1\sigma$.

Moreover, the existence of the Local Hole has been detected in wider cluster distributions, with Böhringer et al. (2015), Collins et al. (2016) and Böhringer, Chon & Collins (2020) finding underdensities of ~ 30 per cent in the X-Ray cluster redshift distributions of the REFLEX II and CLASSIX surveys, respectively. These results are in strong agreement with the galaxy counts of WS14, and suggest that the observed H_0 within the underdensity would be inflated by $5.5^{+2.1}_{-2.8}$ per cent.

Contrastingly, Riess et al. (2018a) critique the assumption of isotropy and spherical symmetry assumed in the modelling of the Local Hole, highlighting that the WS14 data set covers only 20 per cent of the sky, yet measurements drawn from this subset are projected globally to draw conclusions on the entire local environment. These authors further suggest that such an all-sky local underdensity would then be incompatible with the expected cosmic variance of mass density fluctuations in the ΛCDM model at the $\approx 6\sigma$ level. In addition, Kenworthy, Scolnic & Riess (2019) failed to find dynamical evidence in the form of infall velocities for the Local Hole in their Pantheon supernova catalogue.

⋆ E-mail: jonathanhw.wong@gmail.com

Further, through analyses of the galaxy distribution in the 2M++ Catalogue, Jasche & Lavaux ([2019](#)), following Lavaux & Hudson ([2011](#); hereafter LH11) find that local structure can be accommodated within a standard concordance model, with no support for an underdensity on the scale suggested by WS14. However, Shanks et al. ([2019b](#); see also Whitbourn & Shanks [2016](#)) question the choice of the Luminosity Function (LF) parameters used by Jasche & Lavaux ([2019](#)) and LH11.

In this work, we will examine two aspects of the above arguments against the Local Hole. First, to address the premise that the conclusions of WS14 cover too small a sky area to support a roughly isotropic underdensity around our position, we will extend the analysis of WS14 and measure K-band $n(m)$ and $n(z)$ galaxy counts over ≈ 90 per cent of the sky to a limiting Galactic latitude $|b| \gtrsim 5°$.

Secondly, we will compare the $n(z)$ and $n(K)$ model predictions of WS14 with LH11. These predictions will be compared at both the bright 2MASS limit and at the fainter K-band limit of the GAMA survey to try and understand the reasons for the different conclusions of WS14 and LH11 on the existence of the 'Local Hole'.

2 DATA

2.1 Photometric surveys

We now detail properties of the photometric surveys used to provide $n(m)$ counts, alongside calibration techniques and star-galaxy separation methods that we apply to ensure consistency between the photometric data and model fit. Following WS14, we choose to work in the Vega system throughout. Thus for the GAMA survey, we apply a K-band conversion from the AB system according to the relation determined by Driver et al. ([2016](#))

$$K_s(Vega) = K_s(AB) - 1.839 \tag{1}$$

2.1.1 2MASS

The Two Micron All Sky Survey, 2MASS (Skrutskie et al. [2006](#)) is a near-infrared photometric survey achieving a 99.998 per cent coverage of the celestial sphere. In this work, we will take K-band $n(m)$ counts from the 2MASS Extended Souce Catalogue (2MASS_xsc), which is found to be ~ 97.5 per cent complete (McIntosh et al. [2006](#)), with galaxies thought to account for ≈ 97 per cent of sources.

For the galaxy $n(m)$ results, we choose to work in Galactic coordinates and present counts from down to a limiting Galactic latitude $|b| > 5°$ except for the Galactic longitude range, $330 < l < 30°$ where our limit will be $|b| > 10°$. This is the same $37\,063\,\mathrm{deg}^2$ area of sky used by LH11. These cuts are motivated by the increasing density of Galactic stars at lower latitudes and close to the Galactic Centre.

Following WS14, sources are first selected according to the quality tags '$cc\_flg = 0$' or '$cc\_flg = Z$'. We will work with a corrected form of the 2MASS_xsc extrapolated surface brightness magnitude, 'K_m_ext', quoted in the Vega system. The conversion we use is detailed in WS14 Appendix A1, and utilizes the K-band photometry of Loveday ([2000](#)). For sources in the range $10 < K < 13.5$, we take a corrected form of the magnitude, $K\_$Best, defined as

$$K\_\text{Best} = 0.952 \times (K\_m\_ext + 0.5625). \tag{2}$$

The effect of converting to the $K\_$Best system is to slightly steepen the observed counts at the fainter end. However, the effect of the

conversion is small and its inclusion does not alter the conclusions we draw.

To remove stellar sources in 2MASS, we exploit here the availability of the Gaia EDR3 astrometric catalogue (Gaia Collaboration et al. [2016](#), [2021](#)) and simply require that a source detected in Gaia EDR3 is not classed as pointlike as defined by equation (3) of Section [2.1.4](#). But when compared to the star-galaxy separation technique used by WS14, little difference to the galaxy $n(K)$ and $n(z)$ is seen.

Finally, 2MASS galaxy K_s magnitudes are corrected throughout for Galactic absorption using the $E(B - V)$ extinction values determined by Schlafly & Finkbeiner ([2011](#)) and $A_{K_s} = 0.382E(B - V)$. The coefficient here corresponds to the relation $A_V = 3.1E(B - V)$ for the V-band.

2.1.2 GAMA

The Galaxy And Mass Assembly, GAMA survey (Driver et al. [2009](#)) provides a multiwavelength catalogue covering the near- and mid-infrared, comprising $\approx 300\,000$ galaxies over an area of $\approx 180\,\mathrm{deg}^2$. The survey offers deeper K counts which are not accessible in the 2MASS sample, so we will use GAMA to compare the ability of the WS14- and LH11-normalized models to fit faint K-band $n(m)$ counts. Measurements will be taken from the GAMA DR3 release (Baldry et al. [2018](#)) using the Kron magnitude 'MAG_AUTO_K', initially given in the AB system. We will target the combined count of the three equatorial regions G09, G12, and G15, each covering $59.98\,\mathrm{deg}^2$ with an estimated galaxy completeness of ≈ 98.5 per cent (Baldry et al. [2010](#)). We shall take the GAMA sample to be photometrically complete to $K < 15.5$ but only complete to $K < 15$ for their redshift survey since a visual inspection of the K counts of galaxies with redshifts indicates that only the G09 and G12 redshift surveys reach this limit. For star-galaxy separation, we shall first use the $g - i$: $J - K$ galaxy colour-based method recommended for GAMA by Baldry et al. ([2010](#)) (see also Jarvis et al. [2013](#)) before applying the *Gaia* criteria of Section [2.1.4](#) to this subset to reject any remaining stars.

2.1.3 VICS82

VISTA-CFHT Stripe 82, VICS82 (Geach et al. [2017](#)), is a survey in the near-infrared over J and K_s bands, covering $\approx 150\,\mathrm{deg}^2$ of the SDSS Stripe82 equatorial field. The survey provides deep coverage to $K < 20$. Sources are detected and presented measuring a total magnitude '$MAG - AUTO$' quoted in the AB system. The image extraction gives a star-galaxy separation flag, '*Class Star*', with extended and point-like sources distributed at 0 and 1, respectively. Whereas Geach et al. ([2017](#)) defined pointlike sources at *Class Star* > 0.95, we shall define extended objects using a more conservative cut at *Class Star* < 0.9. We then use the *Gaia* method of Section [2.1.4](#) to remove any remaining pointlike objects. In terms of K magnitude calibration, we start from the same VICS82 K_mag_auto system as Geach et al. ([2017](#)) who note that there is zero offset to 2MASS total K_20 magnitudes (see their Fig. [4](#)). However, in Appendix [C](#), we find that between $12.0 < K\_m\_ext < 13.5$, the offset $K\_m\_ext - K\_VICS82 = 0.04 \pm 0.004$ mag and this is the offset we use for these VICS82 data in this work. As with GAMA, we then use the deep K-band counts of VICS82 to test how well the WS14 model predicts faint galaxy counts beyond the 2MASS $K < 13$ limit.

Table 1. Summary statistics of the $n(m)$ and $n(z)$ data sets we use for analysis of the Local Hole over the wide-sky area ($|b| > 5°$ except for $|b| > 10°$ at $330° < l < 30°$).

Survey	Wide-Sky Area (deg^2)	Magnitude limit	$n(m)$ (2MASS)	$n(z)$
2MRS	37 063	$K < 11.5$	41 771	38 730
2M++				34 310
2MRS	37 063	$K < 11.75$	59 997	43 295
2M++				44 152

2.1.4 Star–galaxy separation using Gaia

The Gaia Survey (Gaia Collaboration et al. 2018) provides an all-sky photometry and astrometry catalogue for over 1 billion sources in the *G*-band, and is taken as essentially complete for stars between $G = 12$ and 17. The filter used to determine pointlike objects makes use of the total flux density 'G' and astrometric noise parameter 'A', which is a measure of the extra noise per observation that can account for the scatter of residuals (Lindegren et al. 2018). Explicitly, through the technique of Krolewski et al. (2020), pointlike sources are then classified as

$$\text{pointlike}(G, A)$$
$$= \begin{cases} \log_{10} A < 0.5 & \text{if } G < 19.25 \\ \log_{10} A < 0.5 + \frac{5}{16}(G - 19.25) & \text{otherwise.} \end{cases} \quad (3)$$

This separation technique is applied, sometimes in combination with other techniques, to the raw photometric data sets taken from 2MASS, GAMA, and VICS82 used to analyse the wide-sky and faint-end $n(m)$ counts.

2.2 Redshift surveys

We now present characteristics of the redshift surveys used to measure the $n(z)$ galaxy distribution; and the techniques we apply to ensure the data remain consistent with those of WS14.

To achieve close to all-sky measurement, we similarly take the observed $n(z)$ survey distribution to the same LH11 (l, b) limits discussed in Section 2.1.1 and work with redshifts reduced to the Local Group barycentre (see equation 10 of WS14). While WS14 use the SDSS and 6dFGRS surveys to measure separate distributions in the Northern- and Southern-galactic hemispheres, respectively, we will access a larger sky area using the wide-sky redshift surveys based on the photometric 2MASS catalogue.

2.2.1 2MRS

The 2MASS Redshift Survey, 2MRS (Huchra et al. 2012) is a spectroscopic survey of ~45 000 galaxies covering 91 per cent of the sky built from a selected sample of the 2MASS photometric catalogue limited to $K < 11.75$. The 2MRS Survey is reported to be 97.6 per cent complete excluding the galactic region $|b| < 5°$ and provides a coverage to a depth $z \sim 0.08$.

To remain consistent with the $n(m)$ distributions, we work with a *K*-band limited 2MRS sample, achieved by matching the 2MRS data with the star-separated 2MASS Extended Source Catalogue. To minimize completeness anomalies, we take a conservative cut at $K < 11.5$ to measure the $n(z)$ distribution. In Table 1, we provide summary statistics of the $n(z)$ data set achieved by the matching procedure, alongside the corresponding 2MASS $n(m)$ count.

2.2.2 2M++

The 2M++ Catalogue (LH11) is a spectroscopic survey of ~70 000 galaxies comprised of redshift data from 2MRS, 6dFGRS, and SDSS. The 6dFGRS/SDSS and 2MRS data are given to $|b| > 10°$ and $|b| > 5°$, respectively, except in the region $-30° < l < +30°$ where 2MRS is limited to $|b| > 10°$.

The 2M++ Catalogue applies masks to this field to associate particular regions to each survey, weighting by completeness and magnitude limits. Overall, this creates a set of galaxies covering an all-sky area of 37 080 deg^2 which is thought to be ~ 90 per cent complete to $K \leq 12.5$. To compare with counts from 2MRS, we will measure the redshift distribution to a depth $K < 11.5$, with the summary statistics presented in Table 1.

2.2.3 Spectroscopic incompleteness

For a given $n(z)$ sample taken from 2MRS and 2M++, we correct the data using an incompleteness factor. The observed $n(z)$ distribution from the survey is multiplied by the ratio of the total number of photometric to spectroscopic galaxies within the same target area and magnitude limit. Here, the photometric count is taken from the 2MASS Extended Source Catalogue and the correction ensures that the total number of galaxies considered in the redshift distribution $n(z)$ is the same as in the magnitude count $n(m)$. A breakdown of the completeness of each survey as a function of magnitude is presented in Appendix D.

2.3 Field–field errors

The field–field error, σ, in the galaxy 2D sky or 3D volume density in each photometric or spectroscopic bin is simply calculated by sampling the galaxy densities in n sub-fields within the wide-sky area and calculating their standard error. For n sub-fields, each with galaxy density, ρ_i, the standard error σ on the mean galaxy density, $\bar{\rho}$, in each magnitude or redshift bin is therefore

$$\sigma^2 = \frac{1}{n(n-1)} \sum_{i=1}^{n} (\rho_i - \bar{\rho})^2. \quad (4)$$

So, for the 2MASS wide-sky survey, we divide its area into 20 subfields each covering 1570 deg^2 over the majority of the sky, but in the offset strip for $330° < l < 30°$, there are four additional subfields of equal area 1420 deg^2 that have slightly different boundaries. The 10 per cent smaller boundaries for 4 out of 24 sub-fields is assumed to leave equation (4) a good approximation to the true field–field error estimate. In Section 5, we detail the Galactic coordinate boundaries of each sub-field in a Mollweide projection and consider the individual galaxy densities in each of these $n = 24$ sub-fields to visualize the extent on the sky of the Local Hole.

3 MODELLING

To examine the redshift and magnitude distribution of galaxies, we measure their differential number counts per square degree on the sky as a function of magnitude, m, and redshift, z, over a bin size $\Delta m = 0.5$ and $\Delta z = 0.002$, respectively. The observed counts are then compared to the WS14 theoretical predictions that assumed a model based on the sum of contributions from the type-dependent LFs of Metcalfe et al. (2001). The LF parameters ϕ^*, α, M^*, which represent the characteristic density, slope, and characteristic magnitude, respectively, are presented for each galaxy type in Table 2.

Table 2. The LF parameters defined at zero redshift as a function of galaxy-type, used as the homogeneous model by WS14 and adopted in this work. The absolute magnitudes are 'total' K-band magnitudes, corresponding to our K_Best system. Here, the Hubble parameter $H_0 = 100\,h\,\mathrm{km\,s^{-1}\,Mpc^{-1}}$.

Type	$\phi^*(h^3\,\mathrm{Mpc^{-3}})$	α	$M_K^* + 5\log_{10}(h)$
E/S0	7.42×10^{-3}	-0.7	-23.42
Sab	3.70×10^{-3}	-0.7	-23.28
Sbc	4.96×10^{-3}	-1.1	-23.33
Scd	2.18×10^{-3}	-1.5	-22.84
Sdm	1.09×10^{-3}	-1.5	-22.21

The apparent magnitude of galaxies is further dependent on their spectral energy distribution and evolution, modelled through $k(z)$ and $e(z)$ corrections, respectively. Thus, we calculate the apparent magnitude m by including these in the distance modulus for the $[m, z]$ relation

$$m = M + 5\log_{10}(D_L(z)) + 25 + k(z) + e(z), \tag{5}$$

where $D_L(z)$ represents the luminosity distance at redshift, z. In this work, the k and e corrections are adopted from WS14 who adopt Bruzual & Charlot (2003) stellar synthesis models. We note that the K band is less affected by k and e corrections than in bluer bands because of the older stars that dominate in the near-IR.

In addition to the basic homogeneous prediction, we consider the WS14 inhomogeneous model in which the normalization ϕ^* is described as a function of redshift. We trace the radial density profile shown in each redshift bin of the observed $n(z)$ count (see Fig. 1b), and apply this correction to the $n(m)$ model prediction according to

$$\phi^*(z) = \begin{cases} \frac{n(z)_{\mathrm{obs}}}{n(z)_{\mathrm{global}}}\phi^*_{\mathrm{global}} & z \leq z_{\mathrm{global}}, \\ \phi^*_{\mathrm{global}} & z > z_{\mathrm{global}} \end{cases}, \tag{6}$$

where the $n(z)_{\mathrm{obs}}$ are the observed distributions from our chosen redshift surveys, ϕ^*_{global} describes the standard homogeneous normalization as detailed in Table 2, and z_{global} is the scale at which the inhomogeneous model transitions to the homogeneous galaxy density.

In such a way we can model the effect of large-scale structure in the number-magnitude prediction, which we use as a check for consistency in measurements of any underdensity between the observed $n(m)$ and $n(z)$ counts. In this work, we test the effect of two transition values $z_{\mathrm{global}} = 0.06$ and 0.07.

4 GALAXY REDSHIFT DISTRIBUTION

The observed $n(z)$ distribution measured in the 2MRS and 2M++ catalogues over the wide-sky area to $|b| \gtrsim 5°$ is shown in Fig. 1(a). The data are limited to $K < 11.5$ and compared to the $n(z)$ predictions of the homogeneous WS14 LF model,[1] with a corresponding plot of the observed $n(z)$ divided by the model shown in Fig. 1 (b). Counts have been corrected with the spectroscopic incompleteness factor described in Section 2.2.3; and a description of the completeness of each sample as a function of magnitude is given in Appendix D. Errors have been calculated using the field–field method incorporating the uncertainty in each observed redshift bin combined with the uncertainty in the incompleteness.

---

[1]We note that convolving the WS14 model $n(z)$ with a Gaussian of width $\sigma_z = 0.001$ to represent the combined effect of redshift errors and peculiar velocities of $\pm 300\,\mathrm{km\,s^{-1}}$ shows no discernible difference.

Subject to the limiting magnitude $K < 11.5$, each survey shows a distribution where the majority of the observed $n(z)$ data fall below the predicted count of the WS14 homogeneous model. The observed distributions fail to converge to the model until $z > 0.06$ and below this range the data exhibit a characteristic underdensity that is consistent with $n(z)$ counts over the NGC and SGC presented in WS14.

To analyse the scale of underdensity in our measurements, we consider the 'total' density contrast, calculated by evaluating the difference between the sum of the observed count and predicted count, normalized to the sum of the predicted count. Here, we take the sum over $n(z)$ bins from $z = 0$ to the upper limits of $z = 0.05$ and 0.075. Calculations of the density contrast in our wide-sky 2MRS and 2M++ distributions within these bounds are presented in Table 3.

The measured density contrast of each survey at $z < 0.075$ are in excellent agreement and indicate that the wide-sky $n(z)$ counts are $\sim 21-23$ per cent underdense relative to the model. At both limits, the 2MRS data set produces a marginally greater underdensity than 2M++, however, the two values remain consistent to within 1σ and demonstrate a continuous underdensity in the $n(z)$ distribution.

We note that in our approach, we have applied a single incompleteness factor to correct each bin in the observed $n(z)$ distribution equally while a more detailed examination could incorporate a magnitude-dependent factor. This technique was implemented in WS14, where the completeness factor was introduced into the LF $n(z)$ model such that each bin conserved the galaxy number. However, the change to the $n(z)$ sample as a result of this method was less than 1 per cent and so we have not implemented this more detailed correction here.

We shall return in Section 6.1 to discuss the reasons for the difference in the $n(z)$ model prediction of LH11, also shown in Fig. 1(a).

5 GALAXY NUMBER MAGNITUDE COUNTS

5.1 2MASS $n(m)$ counts

We now consider the 2MASS number-magnitude counts and examine the extent the WS14 homogeneous model can self-consistently replicate an $n(m)$ underdensity that is of the same profile and at a similar depth as that suggested by the galaxy redshift distributions of 2MRS and 2M++ .

The observed K-band $n(m)$ count of the 2MASS Extended Source Catalogue to the wide-sky limit of $|b| \gtrsim 5°$, is presented in Fig. 2(a). Similar to the $n(z)$ comparison in Fig. 1, these counts appear low compared to the homogeneous model of WS14, here at $K < 12$.

To examine whether the $n(m)$ counts are consistent with the form of the underdensity shown in the $n(z)$ measurements, we also predict this $n(m)$ based on the LSS-corrected $\phi^*(z)$ normalization (see Section 3). We first show the observed $n(m)$ count divided by the homogeneous WS14 model in Fig 2(b). Then, we use the $n(z)_{\mathrm{obs}}$ derived from each of the 2MRS and 2M++ $n(z)$ distributions in Fig. 1 (b), both similarly divided by the WS14 homogeneous model. The orange and green lines represent the 2MRS and 2M++ -corrected models, respectively.

At $K < 12.5$, the wide-sky $n(m)$ distribution shows a significant underdensity relative to the homogeneous prediction, only reaching consistency with the model at $K \approx 13$. Moreover, we find that the $\phi^*(z)$ models describing the observed $n(z)$ inhomogeneities in each of 2MRS and 2M++ give a significantly more accurate fit to the 2MASS $n(m)$ count. This indicates that the profile of the underdensity in the galaxy redshift distributions, measured relative to the WS14 homogeneous prediction, is consistent with the observed $n(m)$ counts.
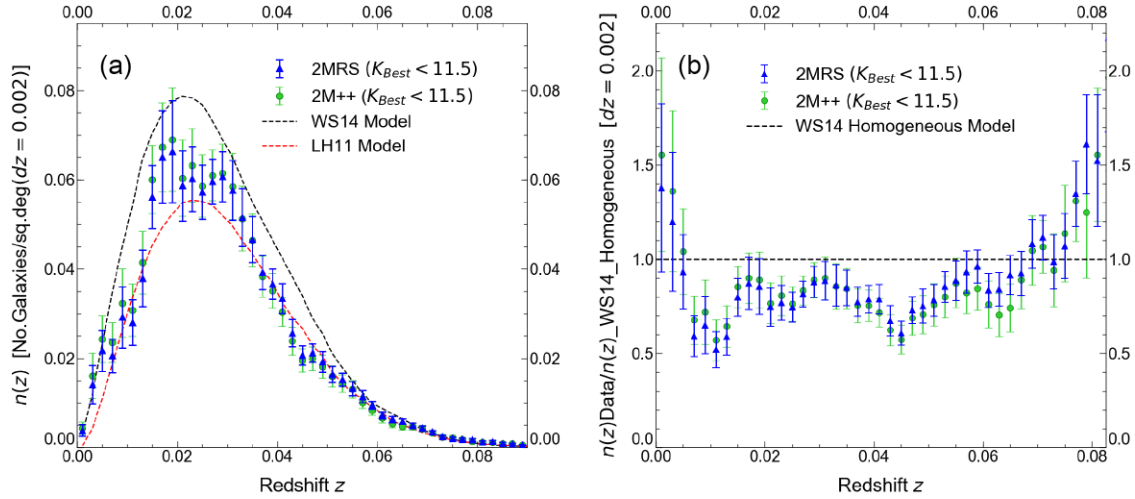
Figure 1. The observed $n(z)$ distributions of the 2MRS and 2M++ Catalogues measured to the wide-sky area $|b| \gtrsim 5°$ and consistently limited to $K < 11.5$ where: (a) Counts are fit alongside the WS14 homogeneous model and LH11-normalized model over a bin size $\Delta z = 0.002$. (b) The $n(z)$ counts are normalized to the WS14 model to demonstrate observed under and overdensities across the distribution.

Table 3. The measured density contrasts between the WS14 LF model and $n(z)$ counts of 2MRS and 2M++ over the $\sim$37 000 deg^2 wide-sky area. The samples are taken to a limiting magnitude $K < 11.5$ and detail the scale of under and overdensities to the specified ranges $z < 0.05$ and $z < 0.075$.

Sample limit	Survey	Density contrast (per cent)
$z < 0.05$	2MRS	-23 ± 2
	2M++	-21 ± 3
$z < 0.075$	2MRS	-22 ± 2
	2M++	-21 ± 2

To explicitly evaluate the 2MASS $n(m)$ underdensity, we give calculations of the density contrast in Table 4. To mitigate the uncertainty at the bright end and remain in line with measurements given by WS14, we take a fixed lower bound, $K > 10$, and vary the upper magnitude bound.

The measurements of the total density contrast in the wide-sky $n(m)$ count in Table 4 demonstrate a significant scale of underdensity at $10 < K < 11.5$ that becomes less pronounced approaching $K \approx 13.5$. Notably, at $K < 11.5$, we measure an underdensity of 20 ± 2 per cent, which is consistent with the $\approx 21 - 22$ per cent underdensity shown in the 2MRS and 2M++ $n(z)$ counts. Additionally, for $K < 12.5$, we find a wide-sky underdensity of 13 ± 1 per cent, which is in good agreement with the 15 ± 3 per cent underdensity calculated in the three WS14 fields over the same magnitude range. The field–field errors suggest strongly significant detections of a 13–21 per cent underdensity over the wide-sky area. This is in agreement with WS14, who found an $\approx$15 per cent underdensity from their sample covering a $\approx$4 times smaller area over the NGC and SGC. In addition, we note the effect of the magnitude calibration to the Loveday system. Excluding the correction lowers the observed count at the faint end by ≈ 10 per cent, confirming the conclusion of WS14 that an underdensity is seen independent of applying the Loveday magnitude correction. Finally, we again shall return in Section 6.1 to discuss why the $n(m)$ model prediction of LH11 also shown in Fig. 2(a) are so much lower than that of WS14.

5.2 Sub-field $n(m)$ density contrast measurements

To further assess the sky extent of the Local Hole, we next consider the properties of the wide-sky sub-fields from which we derive the field–field errors and evaluate the 2MASS $n(m)$ density contrast in each sub-field region.

Fig. 3 shows the density contrast between the 2MASS $n(m)$ counts and the WS14 homogeneous model in each sub-field area that is also used to evaluate the wide-sky $n(m)$ and $n(z)$ field–field errors. The average density contrast in each field is plotted colour-coded on a Mollweide projection, which also details the geometric boundaries of each region in Galactic coordinates.

To probe the underdensity, we choose to take the sum over the range $10 < K < 12.5$ to remain consistent with the limits considered in WS14. In addition, to examine the properties of individual regions, we plot the local galaxy clusters and superclusters highlighted in LH11 using positional data from Abell, Corwin & Olowin (1989), Einasto et al. (1997), and Ebeling et al. (1998), and provide their redshift as quoted by Huchra et al. (2012) in the 2MRS Catalogue.

From the lack of yellow-red colours in Fig. 3, it is clear that underdensities dominate the local Large-Scale Structure across the sky. Now, there are several fields which demonstrate an $n(m)$ count that marginally exceeds the WS14 prediction and we find that such (light green) regions tend to host well-known local galaxy clusters. The 4 out of 24 areas that show an overdensity are those that contain clusters 2,3,4 – Corona Borealis+Bootes+Coma; 6,7 – Shapley + Hydra-Centaurus; 8 – Perseus-Pisces, using the numbering system from Fig. 3. The influence of the structures in these four areas is still not enough to dominate the Local Hole overall 13 ± 1 per cent underdensity in the wide-sky area in Fig. 3.

We conclude that the observed $n(m)$ and $n(z)$ galaxy counts taken to $|b| \gtrsim 5°$ in 2MASS, 2MRS, and 2M++ , show a consistent overall underdensity measured relative to the WS14 model that covers $\approx$90 per cent of the sky. At a limiting depth of $K = 11.5$, the $n(m)$ counts show an underdensity of 20 ± 2 per cent and this scale is replicated in form in the K-limited $n(z)$ distributions at $z < 0.075$ which show an underdensity of $\sim 21 - 22$ per cent.
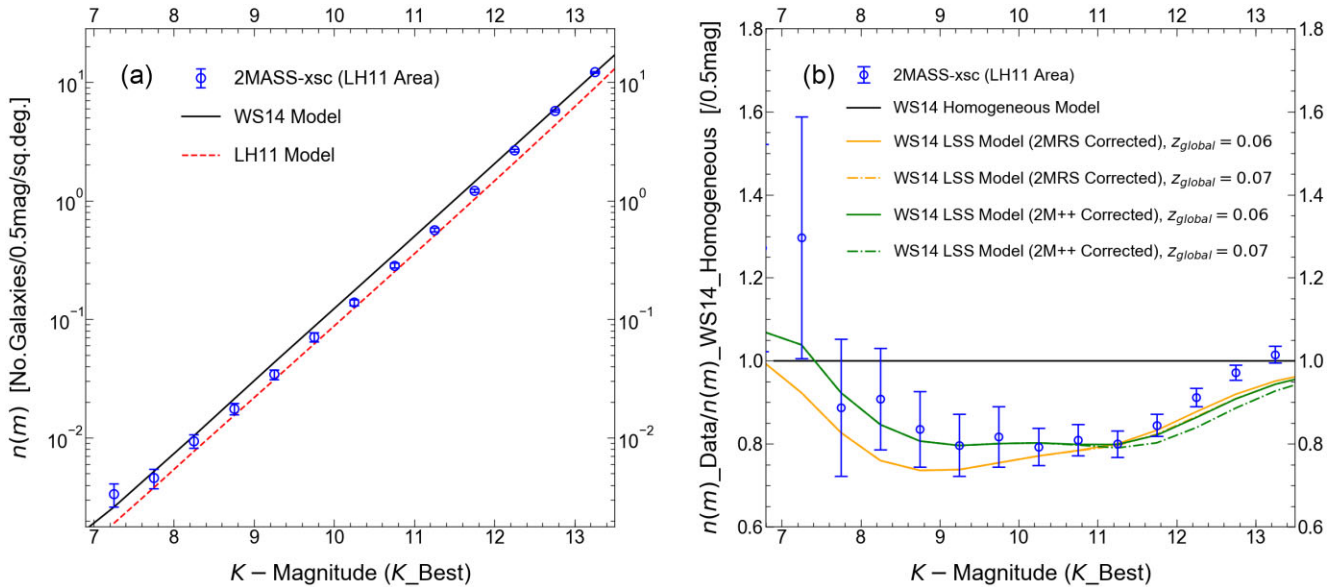
Figure 2. The observed K-band $n(m)$ counts of the 2MASS Extended Source Catalogue taken over the wide-sky region to $|b| \gtrsim 5°$, where: (a) The observed counts are compared to the WS14 and LH11 homogeneous models. (b) The observed counts divided by the WS14 homogeneous model are compared to the inhomogeneous, variable $\phi^*(z)$, versions of the WS14 models based on the 2MRS and 2M++ $n(z)$'s, and similarly divided by the homogeneous WS14 model. The transition to the homogeneous case for both of these inhomogeneous LSS models is investigated for both $z_{\text{global}} = 0.06$ and 0.07.

Table 4. Measurements of the density contrast in the 2MASS wide-sky $n(m)$ counts relative to the WS14 model, taken to various K-limits to examine the extent of underdensities in the distribution. Errors are field–field based on 24 sub-fields.

Sky region	Sample limit	Density contrast (per cent)
$|b| \gtrsim 5°$	$10 < K < 11.5$	-20 ± 2
$|b| \gtrsim 5°$	$10 < K < 12.5$	-13 ± 1
$|b| \gtrsim 5°$	$10 < K < 13.5$	-3 ± 1

6 COMPARISON OF LF AND OTHER MODEL PARAMETERS

The above arguments for the Local Hole underdensity depend on the accuracy of our model LF and to a lesser extent our $k + e$ parameters that are the basis of our $n(z)$ and $n(m)$ models. We note that Whitbourn & Shanks (2016) made several different estimates of the galaxy LF in the K band from the $K < 12.5$ 6dF and SDSS redshift surveys including parametric and non-parametric 'cluster-free' estimators and found good agreement with the form of the LF used by WS14 and in this work. The 'cluster-free' methods are required since they ensure that at least the form of the LF is independent of the local large-scale structure and mitigates the presence of voids as well as clusters. The non-parametric estimators also allowed independent estimates of the local galaxy density profiles to be made and showed that the results of WS14 were robust in terms of the choice of LF model. The WS14 LF normalization was also tested using various methods as described in Section 2.3.1 of Whitbourn & Shanks (2016).

We now turn to a comparison between the WS14 galaxy count predictions with those made by LH11 who failed to find an underdensity in the 2M++ $n(z)$ data. To examine the counts produced by their model, we assume the LF parameters given in their Table 2, where in the Local Group frame with $750 < v < 20\,000\,\text{km s}^{-1}$, they find $\alpha = -0.86$; $M^* = -23.24 + 5\log_{10}(h)$; $\phi^* = 1.13 \times 10^{-2}h^3\text{Mpc}^{-3}$, independent of galaxy type. Note that we brighten the LH11 M^* by

0.19 mag to $M^* = -23.43 + 5\log_{10}(h)$ in our version of their model to account for the 0.19 mag difference between K_m_ext magnitudes used here and the 2MASS $K_{Kron}(= K\_20)$ magnitudes used by LH11 (see Appendix B). In Fig. 4 (a), we compare their $z = 0$ LF with our LF summed over our five galaxy types. Importantly, LH11 note that their fitted LFs show a distinctly flatter faint slope ($\alpha > -1$) than other low redshift LF estimates (see their Fig 7a) that generally look more similar to the steeper WS14 LF (see also Whitbourn & Shanks 2016). However, Fig. 4 (a) shows that the form of both LF's is similar in the range around M^* that dominates in magnitude limited galaxy samples, apart from their normalization, with the LH11 LF appearing ≈ 40 per cent lower than that of WS14. We shall argue that this low normalization is crucial in the failure of LH11 to find the 'Local Hole'.

Next, we compare the $k + e$ - redshift models of LH11 and WS14 in Fig. 4(b). Two $k + e(z)$ models are shown for WS14 representing their early-type model applied to E/S0/Sab and their late type model applied to Sbc/Scd/Sdm. These models come from Bruzual & Charlot (2003) with parameters as described by Metcalfe et al. (2006). At $z = 0.1$, these models give respectively $\Delta_K = -0.28$ and -0.31. We also show just the $k(z)$ for early and late types in Fig. 4. At $z = 0.1$, these $k(z)$ models give respectively $\Delta_K = -0.26$ and -0.25, implying little evolution in the $e(z)$ model for the early types and 0.06 mag for the late types.

We note that LH11 apply their $k + e$ corrections to the data whereas we apply them to the model. So reversing their sign on their $k(z)$ and $e(z)$ terms, the correction we add to our K magnitudes in our count model is

$$\Delta_K(z) = k(z) - e(z). \tag{7}$$

LH11 give $k(z) = -2.1z$ and $e(z) = 0.8z$ giving our additive correction as

$$\Delta_K(z) = k(z) - e(z) = -2.1z - 0.8z = -2.9z, \tag{8}$$

as representing the LH11 k- and evolutionary corrections, giving $\Delta_K = -0.29$ mag at $z = 0.1$. Their second model includes an
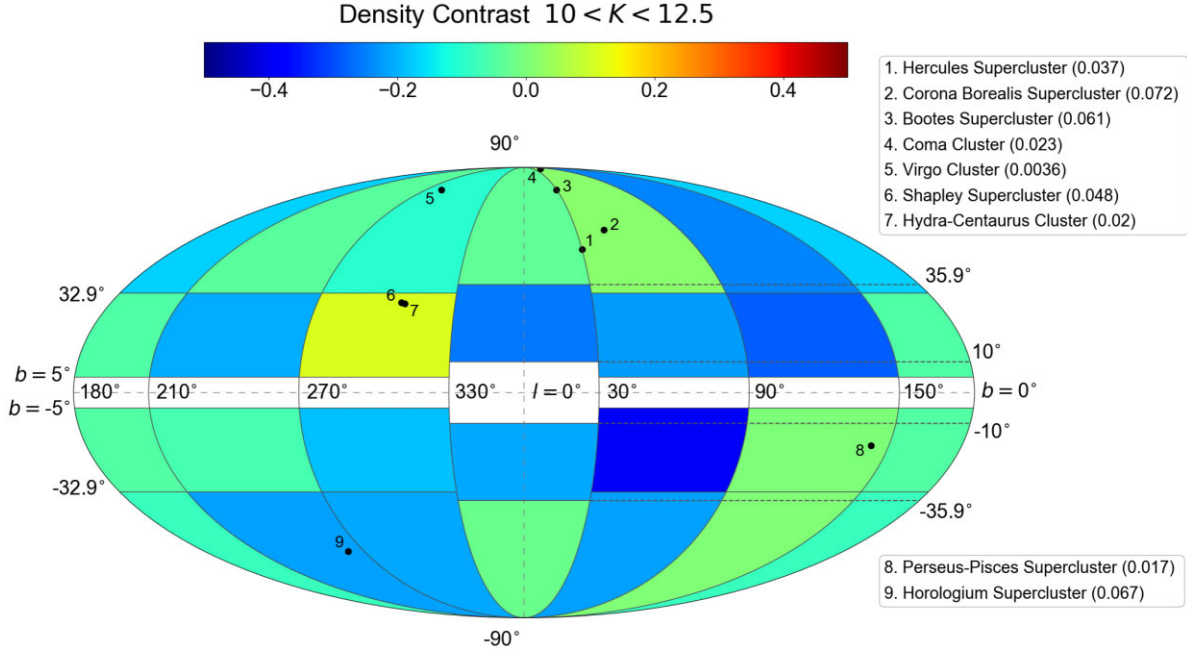
Figure 3. A Mollweide contour plot detailing the galactic coordinate positions of each sub-field we have used to calculate the field–field errors in our wide-sky $n(m)$ and $n(z)$ distributions. In each region, we have evaluated the 2MASS $n(m)$ density contrast, measured at $10 < K < 12.5$, and plotted local galaxy structures to investigate the regional densities. The legend describes the key for each galaxy structure and their corresponding redshift is given in brackets.
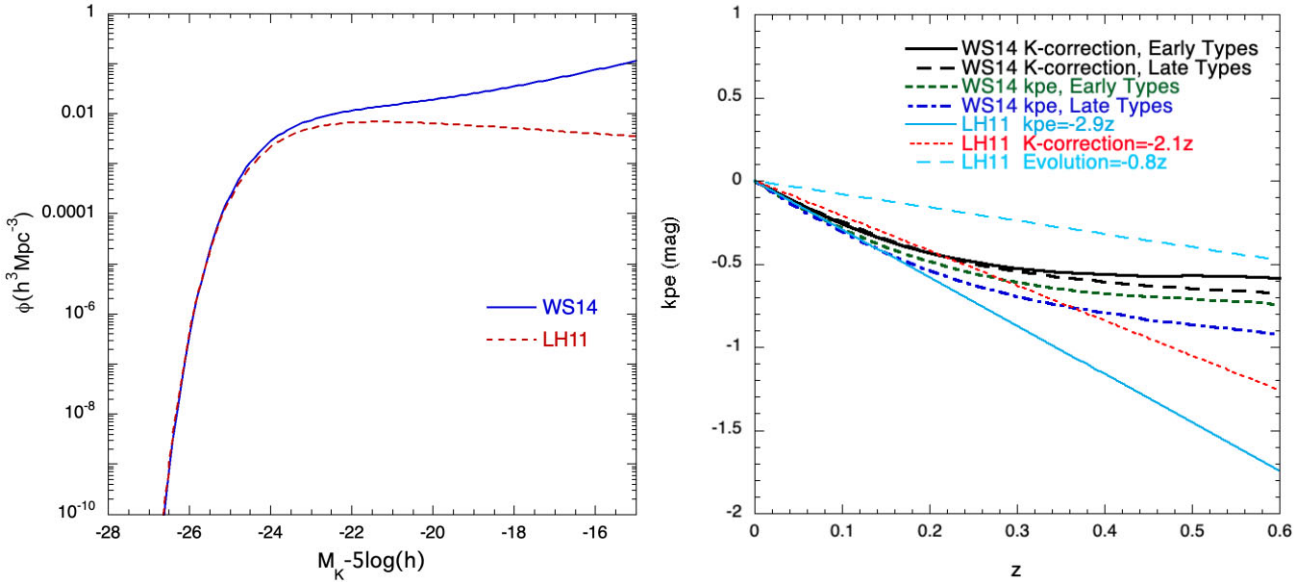

Figure 4. (a) The galaxy K LF of WS14 as used here compared to that of LH11. (b) The k and $k + e$ corrections of WS14 compared to those of LH11, for the K-band.

additional galaxy $(1 + z)^4$ surface brightness dimming correction so in magnitudes is

$$\Delta_K(z) = 0.16(10\log_{10}(1+z)) + 1.16(k(z) - e(z)), \qquad (9)$$

i.e.

$$\Delta_K(z) = 1.6\log_{10}(1+z) - 3.4z \qquad (10)$$

and so $\Delta_K = -0.27$ mag at $z = 0.1$.

Since we are using total K magnitudes, the effect of cosmological dimming of surface brightness is included in our measured magnitudes. So in any comparison of the LH11 model with our K band data, only the $k + e$ terms are used in the model. So at $z = 0.1$, our $k + e$ term is $\Delta_K \approx -0.29$ mag, the same as the $\Delta_K = -0.29$ mag of LH11. Similarly at $z = 0.3$, which is effectively our largest redshift of interest at $K < 15.5$, $z = 0.3$, $\Delta_K \approx -0.60$ to -0.69 mag for the WS14 $k + e$ model compared to $\Delta_K = -0.87$ mag for LH11.
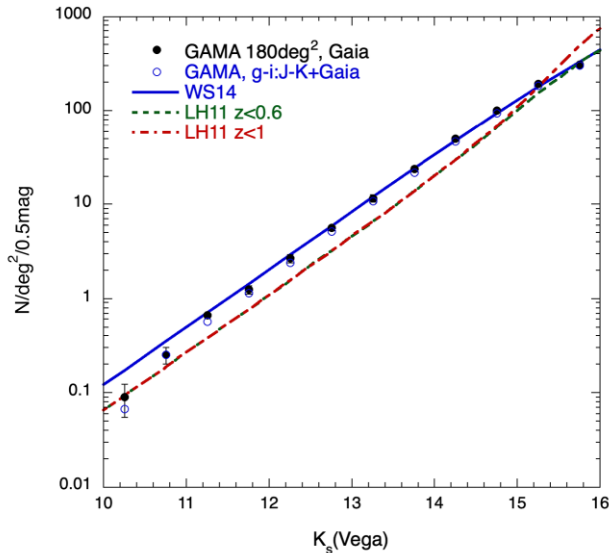
Figure 5. The WS14 and LH11 count models compared to the GAMA survey observed $n(K)$ counts averaged over three fields. Solid circles are the GAMA counts with the Gaia star-galaxy separation and open circles are with the *Gaia* separation applied after star-galaxy separating by colour (Baldry et al. 2010). Two versions of the LH11 model are shown with redshift cuts at $z < 0.6$ and $z < 1.0$ to prevent the model diverging due to an unphysical high redshift tail. Field–field errors based on the three GAMA fields are shown.

6.1 Lavaux & Hudson $n(m)$ and $n(z)$ comparisons to $K = 11.5$

In Figs 1(a) and 2(a), we now compare the LH11 model predictions to those of WS14 for the 2MRS and 2M++ $n(z)$ and 2MASS $n(K)$ distributions. Most notably, we find that the LH11 model produces theoretical $n(K)$ and $n(z)$ counts that are significantly lower than the WS14 counterparts and, if anything, slightly *under*predict the observed wide-sky counts particularly near the peak of the $n(z)$ in Fig. 1(a). The LH11 $n(K)$ model is offset by ≈ 40 per cent from the WS14 $n(K)$ prediction. We also note that the $n(z)$ distribution predicted by LH11 when compared to the 2M++ $n(z)$, limited at $K = 11.5/12.5$ mag, shows excellent agreement (see LH11 Fig. 5). However, in Fig. 2(a), beyond $K > 12.5$, the LH11 $n(K)$ model diverges away from the 2MASS data. In contrast, the WS14 model was found to generate a consistency between the wide-sky $n(K)$ and $n(z)$ distributions and imply a similar underdensity of ≈ 20 per cent at $K < 11.5$. Due to the consistency of the slope in each model at both the bright and faint end of $n(K)$ counts, it is likely that the difference between the LH11 and the WS14 models is caused by the different effective normalization in ϕ^* seen around the break in the LF in Fig. 4.

We further note that when we try to reproduce Fig. 5 of LH11, by combining $n(z)$ model predictions using their LF model parameters for their combined $K < 11.5$ and $K < 12.5$ 2M++ samples covering 13069 and 24011 $\deg^2$, respectively, we find that we reasonably reproduce the form and normalization of their predicted $n(z)$ to a few per cent accuracy. So why the fit of the LH11 model is poorer than in our Fig. 1 (a) than in their Fig. 5 remains unknown. Nevertheless, we accept that their model fits our Fig. 1 (a) $n(z)$ better than the model of WS14.

6.2 Lavaux & Hudson $n(m)$ comparison at $K < 16$

To examine the ability of the LH11 model simultaneously to predict the galaxy $n(K)$ at bright and faint magnitudes, we now compare the LH11 and WS14 models to the fainter $n(K)$ counts of the GAMA survey, shown in Fig. 5. We calculate errors using field–field errors as described in Section 2.3.

To compare the count models, we again assume the LH11 LF parameters from their Table 2, $\alpha = -0.86$; $M^* = -23.24 + 5\log_{10}(h)$ (corrected brighter by 0.19 mag into our system); $\phi^* = 1.13 \times 10^{-2} \, h^3 \, \mathrm{Mpc}^{-3}$. We also assume the $k + e$ term of $\Delta_K = -2.9z$ used by LH11, one cut at $z < 0.6$ and one cut at $z < 1$ as shown by the dashed and dotted lines in Fig. 5.

The two LH11 predictions reasonably fit the bright data at $K < 11$ but lie below the observed GAMA data out to $K \approx 15$, then agreeing with these data at $K \approx 15.5$. In the case of the version cut at $z < 1.0$, the model then rises above the GAMA counts. The model cut at $z < 0.6$ remains in better agreement with these data. But without the redshift cuts, we find that the $\Delta_K = -2.9z$ k + e term used by LH11 would vastly overpredict the observed galaxy count not just at $K > 15.5$ mag but at brighter magnitudes too. This is the usual problem with an evolutionary explanation of the steep count slope at $K < 12$, in that models that fits that slope then invariably overpredict the slope at fainter magnitudes. For an evolutionary model to fit, a strong evolution, either in galaxy density or luminosity (as in the LH11 + WS14 models used here) is needed out to $z < 0.1$ and then something quite close to a no-evolution model is required at $0.1 < z < 1$ in the K band. This is similar to what was found in the b_J-band where strong luminosity evolution is at least more plausible. In K, the evolution is less affected by increasing numbers of young blue stars with redshift and so the evolutionary explanation is even less attractive.

The conclusion that the steep K counts are caused by local large-scale structure rather than evolution is strongly supported by the form of the $n(z)$ seen in Fig. 1 where the pattern of underdensities is quite irregular as expected if dominated by galaxy clustering rather than the smoothly increasing count with z expected from evolution. We have also shown that following the detailed changes in $n(z)$ with redshift to model $\phi^*(z)$ gives a consistent fit to the steep $n(m)$ distribution at $K < 12$. We conclude that unless a galaxy evolution model appears that has the required quick cut-off at $z \approx 0.1$ required simultaneously in the K and b_J counts then the simplest explanation of the steep $n(K)$ slope at bright magnitudes is the large-scale structure we have termed the 'Local Hole'.

These conclusions are confirmed by the GAMA $n(z)$ in the range $10 < K < 15$, averaged over the G09, G12, and G15 fields and compared to the WS14 + LH11 models in Fig. 6. Similar results are seen to those for the GAMA $n(K)$ in Fig. 5 with the WS14 model better fitting these data than the LH11 model that again significantly underestimates the observed $n(z)$. Some hint of an underdensity is seen out to $z \approx 0.12$ in the WS14 model comparison with the observed data but the area covered is only 180 $\deg^2$ so the statistical errors are much larger than for the brighter $K < 11.5$ or $K < 12.5$ 'wide-sky' redshift survey samples.[2]

6.3 VICS82 K count model comparison to $K = 18$

To assess further the LF normalization uncertainties, we present in Fig. 7 the $n(K)$ galaxy counts in the range $12 < K < 18$ over the $\approx 150 \deg^2$ area of the VICS82 survey (Geach et al. 2017). Here, the

---

[2]We note that at the suggestion of a referee, we investigated the 2MASS Photometric Redshift Survey (2MPZ, Bilicki et al. 2014) $n(z)$ over the wide sky area used in Fig. 1 to $K < 13.7$, finding evidence that this underdensity may extend to $z \approx 0.15$. But since this result could be affected by as yet unknown systematics in the 2MPZ photometric redshifts, we have left this analysis for future work.
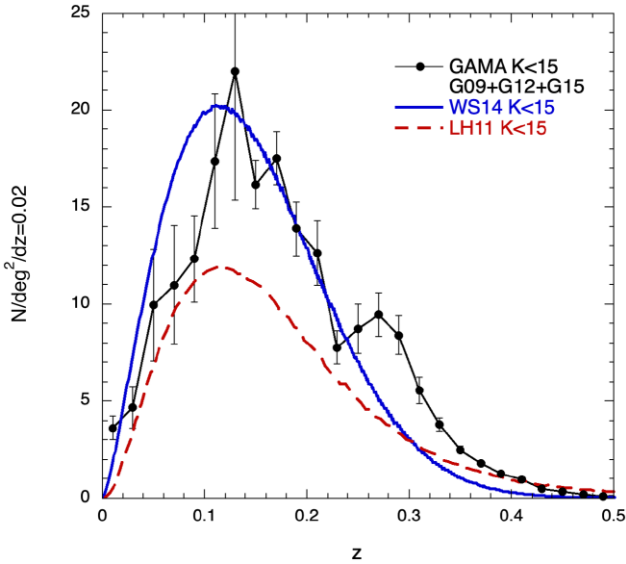
Figure 6. Galaxy $n(z)$ for GAMA survey limited at $10 < K < 15$ and the predictions of the WS14 and LH11 models. We chose the $K < 15$ limit here because this appears to be the effective limit for the K band spectroscopic survey in G09 and G12, although G15 may be complete to a 0.5 mag fainter limit. We note that there is a 'bump' in the GAMA $n(z)$ at $z \approx 0.25$ that appears to have its origin mostly in the G09 and G15 fields with less contribution from G12. G09 and G15 are the two most widely separated fields of the three, arguing that this feature is a statistical fluctuation, if not caused by some z survey target selection issue.
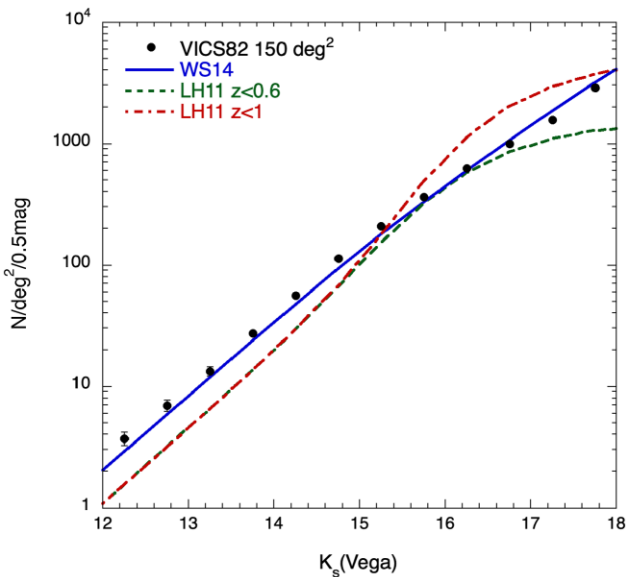
Figure 7. The WS14 and LH11 count models compared to the VICS82 survey (Geach et al. 2017) observed $n(K)$ counts averaged over $\approx 150\,\mathrm{deg}^2$ to $K < 18$. Results are based on star-galaxy separation *Class_Star* < 0.9 with further removal of *Gaia* pointlike objects as defined by equation (3). Field–field errors based on two sub-fields of area 69 and 81 deg^2 are shown. The LH11 models again have redshift cuts at $z < 0.6$ and 1 to prevent divergence due to an unphysical high redshift tail.

faint $K = 18$ limit is 2 mag fainter than the GAMA limit in Fig. 5. Use of the fainter, $K > 18$, VICS82 data to test LF parameters would increasingly depend on the evolutionary model assumed. The bright limit is chosen because the *Class Star* parameter is only calculated by Geach et al. (2017) for $K > 12$ to avoid effects of saturation. The K magnitudes are corrected into the 2MASS K_m_ext system (see Section 2.1.3 and Appendix C). As also described in Section 2.1.3, we have assumed a conservative star-galaxy separation using *Class Star* < 0.9 and then removing any remaining pointlike objects using *Gaia* data and equation (3). We note that there is good agreement with the counts given by Geach et al. (2017) in their fig. 5, once our magnitude offsets are taken into account. In the full range, $12 < K < 16$, we again see excellent agreement with the WS14 model and again the LH11 model significantly underpredicts the galaxy counts. We conclude that, like the GAMA counts, the VICS82 K-band data also strongly support the accuracy of the WS14 model and its LF parameters, from counts based on a completely independent sky area.

6.4 Discussion

What we observe is that the brighter $K < 11.5$ 2MRS $n(z)$ requires a 20 per cent lower ϕ^* than the $K < 15$ GAMA $n(z)$. So good fits to both $n(z)$'s can be obtained if the LF ϕ^* is left as a free parameter (see also Fig. 7 of Sedgwick et al. 2021). This means that the Local Hole may have quite a sharp spatial edge at $z \approx 0.08$ or $r \approx 240h^{-1}$ Mpc. Otherwise, in an evolutionary interpretation this would look more like pure density evolution than luminosity evolution. In the density evolution case, it is true that it would be nearly impossible to differentiate a physical underdensity from a smoothly increasing galaxy density with redshift due to evolution. But the reasonable fit of homogeneous models in the $z < 0.08$ range would again imply that there was a sharp jump in the galaxy density above this redshift. Again this increase in density cannot continue at $z > 0.08$ for the same reason as for pure luminosity evolution, since the counts at higher redshift would quickly be overpredicted. We regard either of these sharply changing evolutionary scenarios around $z \approx 0.08$ as much less likely than an underdensity, as has been argued for some years even on the basis of blue-band number counts (Shanks 1990; Metcalfe et al. 1991).

We highlight the relative normalizations of the WS14 and LH11 LF models as the key outcome of our analysis. The LH11 model fails to fit the faint $n(m)$ galaxy counts in the GAMA survey. If their normalization is correct and no local underdensity exists then it is implied that galaxies must evolve in a way that their space density sharply increases at $z \gtrsim 0.08$ and $K > 12$ and then returns to a non-evolving form out to $z \approx 0.5$ and $K > 20$. This single spurt of evolution at $z \approx 0.08$ has to be seen at similar levels in the b_J, r, and H bands as well as in the K band. It was the unnaturalness of this evolutionary interpretation that originally led e.g. Shanks (1990) to normalize their LF estimates at $b_J (\sim g) > 17$ mag rather than at brighter magnitudes where the form of the LF was estimated. Even authors who originally suggested such an evolutionary explanation (e.g. Maddox et al. 1990) have more recently suggested that a large-scale structure explanation was more plausible (e.g. Norberg et al. 2002). Moreover, WS14 have presented dynamical evidence for a local outflow in their analysis of the relation between $\bar{z}$ and m and Shanks et al. (2019a,b) have shown that this outflow is consistent with the Local Hole underdensity proposed here. It will also be interesting to see whether future all-sky SNIa supernova surveys confirm this $\bar{z} : m$ outflow evidence, based as it is on the assumption that the K-band LF is a reasonable standard candle.

We suggest that the crucial issue for LH11 and Sedgwick et al. (2021) is that they have fitted their LF parameters and particularly the LF normalization in the volume dominated by the Local Hole and thus calibrated out the underdensity. Certainly, their $n(K)$ and $n(z)$ models clearly fail at magnitudes and redshifts just outside the ranges where they have determined their LF parameters. These authors would need to show powerful evidence for the $z < 0.1$ evolution spurt in the favoured ΛCDM model before their rejection of the Local Hole hypothesis could be accepted. In the absence of such a model, the balance of evidence will clearly favour the Local Hole hypothesis.

7 CONCLUSIONS

In this work, we have examined the local galaxy distribution and extended the work of WS14 by measuring observed number-redshift $n(z)$ and number-magnitude $n(m)$ galaxy counts in the K-band across ≈ 90 per cent of the sky down to a Galactic latitude $|b| \gtrsim 5°$.

The $n(z)$ distributions from the 2MRS and 2M++ surveys to $K <$ 11.5 were compared to the homogeneous model of WS14 (see also Metcalfe et al. 2001, 2006). These wide-sky $n(z)$ distributions showed excellent agreement and implied an underdensity of 22 ± 2 per cent relative to the model at $z < 0.075$. We also find that the 2MASS K counts show a similar underdensity of 20 ± 2 per cent at $K < 11.5$ relative to the same model, only converging to the predicted count at $K \approx 13.5$. In addition, an LSS-corrected $\phi^*(z)$ model based on the $n(z)$ distribution, when compared to the 2MASS K counts, showed a much improved fit, confirming the consistency of the 2MASS $n(m)$ and the 2MRS/2M++ $n(z)$ in detecting this underdensity relative to the WS14 model. We also found the underdensity covered 20/24 or ≈ 83 per cent of the observable wide-sky with only areas containing the Shapley and other superclusters and rich clusters like Coma showing up as over- rather than an underdensities.

Combined, our $n(m)$ and $n(z)$ counts are in good agreement with the work of WS14, Frith et al. (2003), Busswell et al. (2004), and Keenan, Barger & Cowie (2013), who find overall underdensities of the order $\approx 15−25$ per cent using a similar galaxy counts method. We also recall that in the $\approx 9000\,deg^2$ sky area analysed by WS14, the underdensity patterns found in redshift were confirmed in detail by the distribution traced by X-ray galaxy clusters in the same volume (Böhringer et al. 2020).

To examine whether our measured underdensity represents a physical Local Hole in the galaxy environment around our observer location requires a confirmation of the accuracy of the WS14 galaxy count model. We have investigated this by comparing the model's predictions for the fainter K galaxy counts from the GAMA and VICS82 surveys. We have also compared these data with the model predictions of LH11 who failed to find an underdensity in the 2M++ survey.

The $n(m)$ and $n(z)$ counts predicted by the LH11 model are lower by ≈ 40 per cent compared to the WS14 model; the LH11 model, thus, initially appears to underpredict the observed wide-sky $n(K)$ and $n(z)$ distributions from 2MASS, 2MRS, and 2M++ . Then, at $K > 13.5$, beyond the 2MASS sample range, the WS14 prediction fits very well the observed $n(K)$ and $n(z)$ counts in the GAMA survey and the observed $n(K)$ in the VICS82 survey. However, the LH11 model shows a consistently poor fit over both the full GAMA + VICS82 $n(K)$ and GAMA $n(z)$ distributions. Thus, the GAMA + VICS82 results indicate that the WS14 model can more accurately fit deep K-counts than the LH11 model, supporting its use in interpreting the lower redshift, wide-sky surveys.

Consequently, our analyses here support the existence of the 'Local Hole' underdensity over ≈ 90 per cent of the sky. At the limiting magnitude $K < 11.5$, the underdensity of 20 ± 2 per cent in the $n(z)$ counts corresponds to a depth of $\approx 100h^{-1}$ Mpc, while the 13 ± 1 per cent underdensity at $K < 12.5$ in the 2MASS wide-sky $n(m)$ counts, that is in good agreement with WS14, would imply the underdensity extends further to a depth of $\approx 150h^{-1}$Mpc. We note that the statistical error on our LF normalization can be easily estimated from the field-to-field errors in the $10 < K < 15$ galaxy counts between the three GAMA fields (see Table A1) and this gives an error of ± 3.4 per cent. The error estimated from the two VICS82 sub-fields would be similar at ± 3.6 per cent in the range $12 < K < 16$, decreasing to ± 1.1 per cent in the range $12 < K < 18$. Combining the GAMA ± 3.4 per cent error with the ± 2 per cent error on the $–20$ per cent underdensity to $K < 11.5$ mag gives the full uncertainty on the Local Hole underdensity out to $100\,h^{-1}$ Mpc to be $−20 \pm 3.9$ per cent i.e. a 5.1σ detection. Similarly the Local Hole $K < 12.5$ underdensity out to $\approx 150h^{-1}$ Mpc is a $−13 \pm 3.5$ per cent or a 3.7σ detection.

Such a 13–20 per cent underdensity at $\approx 100–150\,h^{-1}$Mpc scales would notably affect distance scale measurements of the expansion rate H_0. We can calculate this by assuming the linear theory discussed in WS14 and Shanks et al. (2019a), where $\delta H_0/H_0 = -\frac{1}{3}\,\delta\rho_g/\rho_g \times \Omega_m^{0.6}/b$. Here, we take the galaxy bias $b \approx 1.2$ for K−selected 2MRS galaxies in the standard model (see e.g. Boruah, Hudson & Lavaux 2020; also Maller et al. 2005; Frith, Outram & Shanks 2005b although these latter b values should be treated as upper limits since they apply to $K < 13.5$ and bias is expected to rise with redshift.) From our measured $n(m)$ and $n(z)$ underdensities, this would produce a decrease in the local value of H_0 of $\approx 2−3$ per cent.

We finally consider the significance of such a large-scale inhomogeneity within the standard cosmological model. Frith, Metcalfe & Shanks (2006) created mock 2MASS catalogues from the Hubble Volume simulation to determine theoretically allowed fluctuations and found that a 1σ fluctuation to $H = 13$ ($K \approx 12.5$) over 65 per cent of the sky corresponded to ± 3.25 per cent. Scaling this to the 90 per cent wide-sky coverage used here implies $1\sigma = 2.8$ per cent. Given our 13 ± 3.5 per cent underdensity to $K < 12.5$, we can add in quadrature this ± 2.8 per cent expected fluctuation from the ΛCDM model to obtain 13 ± 4.5 per cent with the error now including our measurement error and the expected count fluctuation expected out to $\approx 150\,h^{-1}$ in ΛCDM. The Local Hole with a 13 per cent underdensity therefore here corresponds to a 2.9σ deviation from what is expected in a ΛCDM cosmology.

If we scale this from $K < 12.5$ mag to $K < 11.5$ mag via a 3D version of equation (3) of Frith, Shanks & Outram (2005a), a 1σ fluctuation at $K < 11.5$ corresponds to ± 5.6 per cent. At $K < 12.5$, the underdensity is $−20 \pm 2$ per cent and folding in the ± 3.4 per cent normalization error gives $−20 \pm 3.9$ per cent or a 5.1σ detection of the Local Hole underdensity. Then adding in the ± 5.6 per cent expected fluctuation amplitude just calculated gives $−20 \pm 6.8$ per cent, implying again a 2.9σ deviation in the ΛCDM cosmology, similar to the $K < 11.5$ case.

However, the deviation from ΛCDM is likely to be more significant. For example, if we normalized our model via the VICS82 $n(K)$ counts in the $12 < K < 18$ range (see Fig. 7) then this would argue that our LF normalization should be still higher and the field–field error would also be lower at ± 1.1 per cent. Additionally, taking into account the excellent fit of the WS14 model to the 2MASS wide-sky data itself at $12.5 < K < 13.5$ (see Fig. 2) would also further increase the significance of the deviation from ΛCDM.

Although the Hubble Volume mocks of Frith et al. (2006) have tested our methodology in the context of an *N*-body simulation 'snapshot' with an appropriate galaxy clustering amplitude in volumes similar to those sampled here, it would be useful to make further tests in a more realistic simulation. For example, a full light-cone analysis could be made, applying our selection cuts in a mock that includes a full 'semi-analytic' galaxy formation model (e.g. Sawala et al. 2022). This would make a further direct test of our methodology while checking if there is any evolutionary effect that provides the spurt of density evolution at $z \approx 0.08$ required to provide an alternative to our large-scale clustering explanation of the Local Hole.

We therefore anticipate that further work to separate out the effects of evolution and LSS on the LF in each of the WS14 and LH11 approaches will shed further light on the presence and extent of the Local Hole. Similarly, further work will be needed to resolve the discrepancy between the detection of dynamical infall at the appropriate level implied from the Local Hole underdensity found by WS14, Shanks et al. (2019a,b) as compared to the lack of such infall found by Kenworthy et al. (2019) and Sedgwick et al. (2021). But here we have confirmed that the proposed Local Hole underdensity extends to cover almost the whole sky and argued that previous failures to find the underdensity are generally due to homogeneous number count models that assume global LF normalizations that are biased low by being determined within the Local Hole region itself.

Finally, if the form of the galaxy $n(K)$ and $n(z)$ do imply a 'Local Hole' then how could it fit into the standard ΛCDM cosmology? Other authors have suggested possibilities to explain unexpectedly large-scale inhomogeneities such as an anisotropic Universe (e.g. Secrest et al. 2021). However, it is hard to see how such suggestions retain the successes of the standard model in terms of the CMB power spectrum etc. We note that other anomalies in the local galaxy distribution exist e.g. Mackenzie et al. (2017) presented evidence for a coherence in the galaxy redshift distribution across $\approx 600\,h^{-1}$ Mpc of the Southern sky out to $z \approx 0.1$. Prompted by this result and by the 'Local Hole' result reported here, Callow et al. (in preparation) will discuss the possibilities that arise if the topology of the Universe is not simply connected. We emphasize that there is no proof but here we just use this model as an example of one that might retain the basic features of the standard model while producing a larger than expected coherent local under or overdensity. It will be interesting to look for other models that introduce such 'new physics' to explain the local large-scale structure while simultaneously reducing the tension in Hubble's Constant.

DATA AVAILABILITY

The 2MASS, 2MRS, 6dF, SDSS, GAMA, VICS82, and *Gaia* data we have used are all publicly available. All other data relevant to this publication will be supplied on request to the authors.

REFERENCES

Abell G. O., Corwin Harold G. J., Olowin R. P., 1989, ApJS, 70, 1
Baldry I. K. et al., 2010, MNRAS, 404, 86
Baldry I. K. et al., 2018, MNRAS, 474, 3875
Bilicki M., Jarrett T. H., Peacock J. A., Cluver M. E., Steward L., 2014, ApJS, 210, 9
Böhringer H., Chon G., Bristow M., Collins C. A., 2015, A&A, 574, A26
Böhringer H., Chon G., Collins C. A., 2020, A&A, 633, A19
Boruah S. S., Hudson M. J., Lavaux G., 2020, MNRAS, 498, 2703
Bruzual G., Charlot S., 2003, MNRAS, 344, 1000
Busswell G. S., Shanks T., Frith W. J., Outram P. J., Metcalfe N., Fong R., 2004, MNRAS, 354, 991
Collins C. A., Böhringer H., Bristow M., Chon G., 2016, in van de Weygaert R., Shandarin S., Saar E., Einasto J., eds, IAU Symp. Vol. 308, The Zeldovich Universe: Genesis and Growth of the Cosmic Web. Cambridge Core, Cambridge, p. 585
Driver S. P. et al., 2009, Astron. Geophys., 50, 5.12
Driver S. P. et al., 2016, MNRAS, 455, 3911
Ebeling H., Edge A. C., Bohringer H., Allen S. W., Crawford C. S., Fabian A. C., Voges W., Huchra J. P., 1998, MNRAS, 301, 881
Einasto M., Tago E., Jaaniste J., Einasto J., Andernach H., 1997, A&AS, 123, 119
Frith W. J., Busswell G. S., Fong R., Metcalfe N., Shanks T., 2003, MNRAS, 345, 1049
Frith W. J., Metcalfe N., Shanks T., 2006, MNRAS, 371, 1601
Frith W. J., Outram P. J., Shanks T., 2005b, MNRAS, 364, 593
Frith W. J., Shanks T., Outram P. J., 2005a, MNRAS, 361, 701
Gaia Collaboration et al., 2016, A&A, 595, A1
Gaia Collaboration et al., 2018, A&A, 616, A1
Gaia Collaboration et al., 2021, A&A, 649, A1
Geach J. E. et al., 2017, ApJS, 231, 7
Huchra J. P. et al., 2012, ApJS, 199, 26
Jarvis M. J. et al., 2013, MNRAS, 428, 1281
Jasche J., Lavaux G., 2019, A&A, 625, A64
Keenan R. C., Barger A. J., Cowie L. L., 2013, ApJ, 775, 62
Kenworthy W. D., Scolnic D., Riess A., 2019, ApJ, 875, 145

Krolewski A., Ferraro S., Schlafly E. F., White M., 2020, J. Cosmol. Astropart. Phys., 2020, 047

Lavaux G., Hudson M. J., 2011, MNRAS, 416, 2840 (LH11)

Lindegren L. et al., 2018, A&A, 616, A2

Loveday J., 2000, MNRAS, 312, 557

Mackenzie R., Shanks T., Bremer M. N., Cai Y.-C., Gunawardhana M. L. P., Kovács A., Norberg P., Szapudi I., 2017, MNRAS, 470, 2328

Maddox S. J., Sutherland W. J., Efstathiou G., Loveday J., Peterson B. A., 1990, MNRAS, 247, 1P

Maller A. H., McIntosh D. H., Katz N., Weinberg M. D., 2005, ApJ, 619, 147

McIntosh D. H., Bell E. F., Weinberg M. D., Katz N., 2006, MNRAS, 373, 1321

Metcalfe N., Shanks T., Campos A., McCracken H. J., Fong R., 2001, MNRAS, 323, 795

Metcalfe N., Shanks T., Fong R., Jones L. R., 1991, MNRAS, 249, 498

Metcalfe N., Shanks T., Weilbacher P. M., McCracken H. J., Fong R., Thompson D., 2006, MNRAS, 370, 1257

Norberg P. et al., 2002, MNRAS, 336, 907

Planck Collaboration et al., 2018, A&A, 641, 67

Riess A. G. et al., 2016, ApJ, 826, 56

Riess A. G. et al., 2018b, ApJ, 861, 126

Riess A. G., Casertano S., Kenworthy D., Scolnic D., Macri L., 2018a, preprint (arXiv:1810.03526)

Sawala T., McAlpine S., Jasche J., Lavaux G., Jenkins A., Johansson P. H., Frenk C. S., 2022, MNRAS, 509, 1432

Schlafly E. F., Finkbeiner D. P., 2011, ApJ, 737, 103

Secrest N. J., von Hausegger S., Rameez M., Mohayaee R., Sarkar S., Colin J., 2021, ApJ, 908, L51

Sedgwick T. M., Collins C. A., Baldry I. K., James P. A., 2021, MNRAS, 500, 3728

Shanks T., 1990, in Bowyer S., Leinert C., eds, IAU Symp. Vol. 139, The Galactic and Extragalactic Background Radiation. Dordrecht, Kluwer, p. 269

Shanks T., Hogarth L. M., Metcalfe N., 2019a, MNRAS, 484, L64

Shanks T., Hogarth L. M., Metcalfe N., Whitbourn J., 2019b, MNRAS, 490, 4715

Skrutskie M. F. et al., 2006, AJ, 131, 1163

Whitbourn J. R., Shanks T., 2014, MNRAS, 437, 2146 (WS14)

Whitbourn J. R., Shanks T., 2016, MNRAS, 459, 496

APPENDIX A: GAMA-2MASS MAGNITUDE COMPARISON

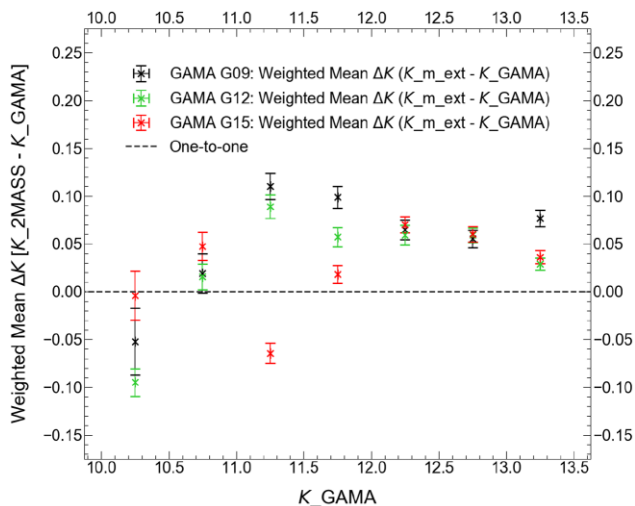We first show Fig. A1, where GAMA *MAG_AUTO_K* and 2MASS

Figure A1. Differences between 2MASS *K_m_ext* and GAMA *MAG_AUTO_K* as a function of GAMA magnitudes for each GAMA field.

Table A1. The magnitude offsets needed to correct the GAMA *MAG_AUTO_K* (= *K_GAMA*) in each of the GAMA fields into the 2MASS *K_BEST* and *K_m_ext* systems. They were calculated by taking an error weighted mean of the magnitude differences in $10 < K_{GAMA} < 13.5$ mag.

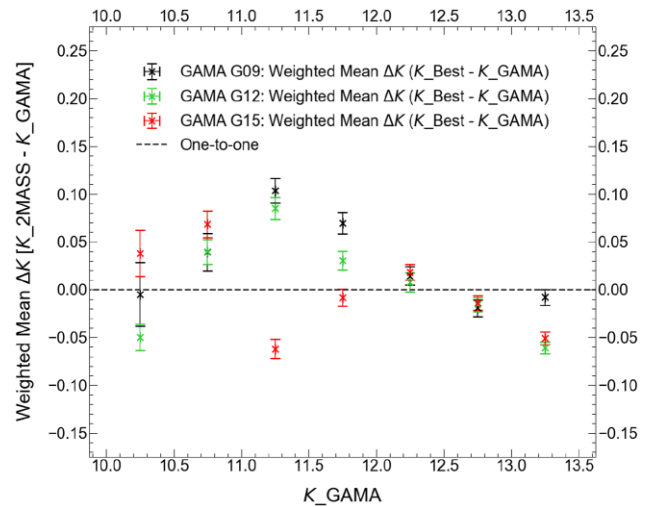| GAMA Field	N (2MASS × GAMA)	Weighted mean $K_{Best} - K_{GAMA}$	Weighted mean $K\_m\_ext - K_{GAMA}$
G09	876	0.019 ± 0.004	0.071 ± 0.004
G12	1208	-0.011 ± 0.003	0.039 ± 0.004
G15	1184	-0.017 ± 0.004	0.033 ± 0.004

Figure A2. Differences between 2MASS *K_BEST* and GAMA *MAG_AUTO_K* as a function of GAMA magnitudes.

K_m_ext magnitudes are directly compared. Table A1 shows the error weighted mean of the differences between these two for each GAMA field within the range $10 < K\_GAMA < 13.5$ mag. Similarly, Fig. A2 shows the comparison between GAMA *MAG_AUTO_K* and 2MASS magnitudes and Table A1 again shows the error weighted mean of the differences for each field in the same *K_GAMA* range.

Following WS14, we have conservatively corrected the GAMA magnitudes for each of the three fields by correcting the GAMA magnitudes by adding the 2MASS *K_m_ext* magnitude offsets given in the fourth column of Table A1 rather than the 2MASS *k_BEST* offsets given in the third column. This takes the GAMA magnitudes into the 2MASS *K_m_ext* system rather than the *K_BEST* system we are actually using. Clearly, if we used the *K_BEST* offsets the GAMA *K* counts would lie even higher in Fig. 5.

APPENDIX B: 2MASS MAGNITUDE COMPARISON

Here, we compare the 2MASS magnitude system, *K_m_ext*, on which our and WS14 *n(K)* results are based with the 2MASS *K_20*(= *K_Kron*) magnitudes used by LH11. The comparisons are shown as a function of *K_m_ext* in Table B1 and Fig. B1. The overall difference is found to be $K\_m\_ext - K\_20 = 0.19 \pm 0.0002$ mag.

Table B1. The 2MASS magnitude offsets between the K_m_ext magnitudes on which WS14 and our magnitudes are based and the K_20 magnitudes used by LH11 (see Fig. B1).

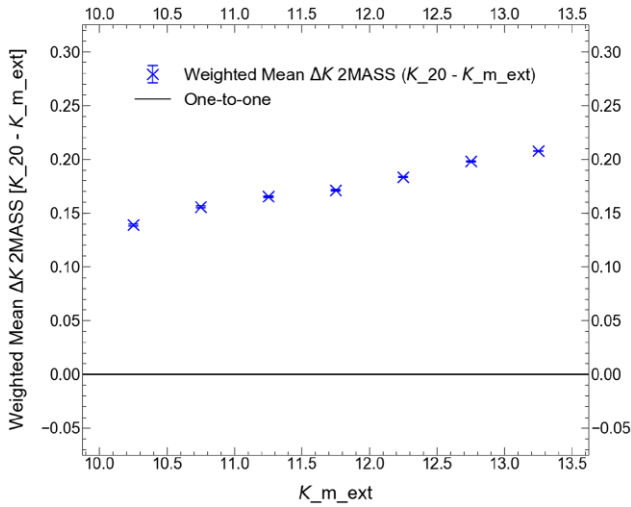| Magnitude range	N_{gal} 2MASS	Weighted mean $K\_m\_ext - K\_20$
$10.0 < K\_m\_ext < 10.5$	4859	0.139 ± 0.0008
$10.5 < K\_m\_ext < 11.0$	9827	0.156 ± 0.0007
$11.0 < K\_m\_ext < 11.5$	18846	0.166 ± 0.0006
$11.5 < K\_m\_ext < 12.0$	38756	0.171 ± 0.0005
$12.0 < K\_m\_ext < 12.5$	81227	0.184 ± 0.0004
$12.5 < K\_m\_ext < 13.0$	169857	0.198 ± 0.0004
$13.0 < K\_m\_ext < 13.5$	359686	0.208 ± 0.0003
$10.0 < K\_m\_ext < 13.5$	683958	0.188 ± 0.0002

Figure B1. The 2MASS magnitude offsets from Table B1 between the K_m_ext magnitudes on which WS14 and our magnitudes are based and the K_20 magnitudes used by LH11.

APPENDIX C: 2MASS-VICS82 MAGNITUDE COMPARISON

Table C1 and Fig. C1 show the offsets between the K_m_ext and VICS82 MAG_AUTO magnitude systems. Because of the possibility of saturation affecting the VICS82 magnitudes at $K < 12.5$

Table C1. The offsets between the 2MASS K_m_ext magnitudes on which WS14 and our magnitudes are based and the VICS82 MAG_AUTO magnitudes used by Geach et al. (2017) (see Fig. C1).

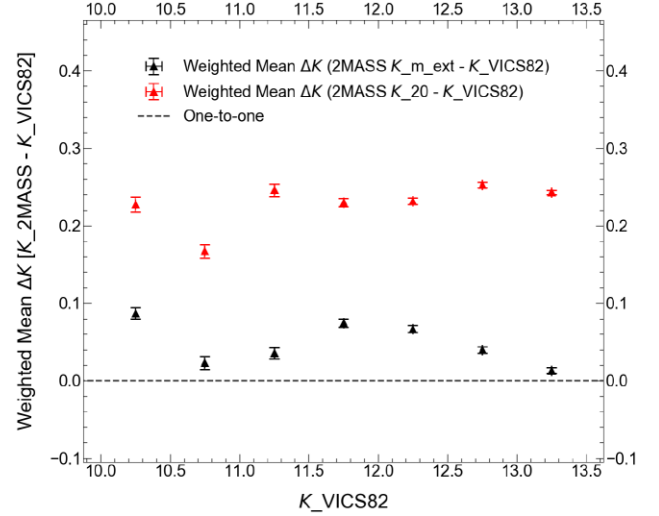| Magnitude range	$Ngal$ 2MASS×VICS82	Weighted mean $K\_m\_ext - K\_VICS82$
$10.0 < K\_m\_ext < 10.5$	26	0.087 ± 0.007
$10.5 < K\_m\_ext < 11.0$	31	0.023 ± 0.009
$11.0 < K\_m\_ext < 11.5$	73	0.036 ± 0.007
$11.5 < K\_m\_ext < 12.0$	175	0.075 ± 0.005
$12.0 < K\_m\_ext < 12.5$	361	0.067 ± 0.005
$12.5 < K\_m\_ext < 13.0$	730	0.040 ± 0.004
$13.0 < K\_m\_ext < 13.5$	1536	0.013 ± 0.004
$10.0 < K\_m\_ext < 13.5$	2932	0.044 ± 0.002

Figure C1. The offsets between the 2MASS K_m_ext magnitudes on which WS14 and our magnitudes are based and the VICS82 MAG_AUTO magnitudes used by Geach et al. (2017) (see Table C1).

and poor S/N affecting the fainter 2MASS magnitudes, we simply average the three values in the range $12.5 < K\_m\_ext < 13.5$ to obtain the overall offset $K\_m\_ext - K\_VICS82 = 0.040 \pm 0.004$ mag as used in Section 2.1.3.

APPENDIX D: SPECTROSCOPIC INCOMPLETENESS OF $n(z)$ COUNTS

In Fig. D1, we present the calculation of the spectroscopic incompleteness factors applied to 2MRS and 2M++ $n(z)$ data before fitting to the WS14 homogeneous model. The $n(z)$ samples are matched to the 2MASS Extended Source Catalogue; and we plot the ratio of the
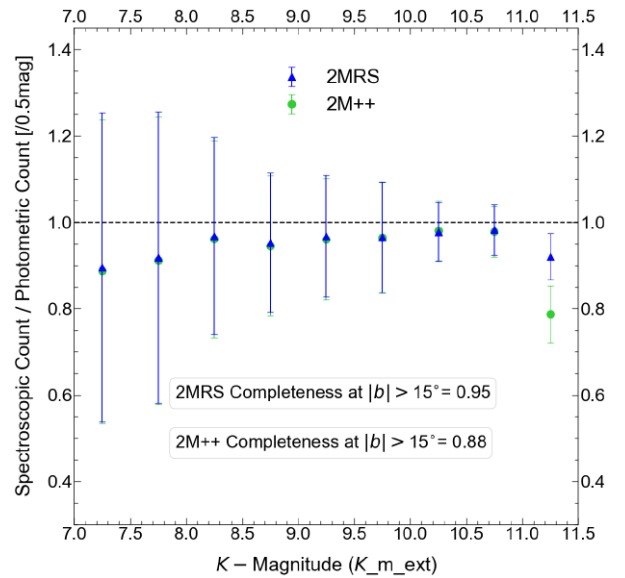

Figure D1. The K-band spectroscopic completeness of 2MRS and 2M++ with respect to the 2MASS Extended Source Catalogue, evaluated per half magnitude bin to the limit $K < 11.5$. Errors have been calculated using the field–field method.

$n(z)$ galaxy count to the 2MASS galaxy count, per half magnitude bin.

The overall completeness of each survey is calculated by the total sum of spectroscopic sources in either 2MRS or 2M++, divided by the total sum of photometric sources in 2MASS taken over the full magnitude range. We measure a completeness of 95 per cent in 2MRS and 88 per cent in 2M++, and the reciprocal of these values is the spectroscopic incompleteness factor which is multiplied to the raw $n(z)$ data of each survey.

This paper has been typeset from a TeX/LaTeX file prepared by the author.